Acta Cryst E CRYSTALLOGRAPHIC COMMUNICATIONS

ISSN 2056-9890

4-Nitrobenzyl 3,4-bis(acetyloxy)-2-(4-methoxyphenyl)pyrrolidine-1-carboxylate: crystal structure, Hirshfeld surface analysis and computational chemistry

Sofia Dallasta Pedroso,[a] Ignez Caracelli,[b]* Julio Zukerman-Schpector,[a] Monica Soto-Monsalve,[c] Regina H. De Almeida Santos,[c] Carlos Roque D. Correia,[d] Ariel L. Llanes Garcia,[d] Huey Chong Kwong[e] and Edward R. T. Tiekink[e]‡

[a]Laboratório de Cristalografia, Esterodinâmica e Modelagem Molecular, Departamento de Química, Universidade Federal de São Carlos, 13565-905 São Carlos, SP, Brazil, [b]Departmento de Física, Universidade Federal de São Carlos, 13565-905 São Carlos, SP, Brazil, [c]Instituto de Química de São Carlos, Universidade de São Paulo, São Carlos, SP, Brazil, [d]Instituto de Química, Universidade Estadual de Campinas, UNICAMP, C.P. 6154, CEP 13084-917 Campinas, Brazil, and [e]Research Centre for Crystalline Materials, School of Science and Technology, Sunway University, 47500 Bandar Sunway, Selangor Darul Ehsan, Malaysia. *Correspondence e-mail: ignez@df.ufscar.br

Received 10 June 2020
Accepted 11 June 2020

Edited by W. T. A. Harrison, University of Aberdeen, Scotland

‡ Additional correspondence author, e-mail: edwardt@sunway.edu.my.

Keywords: crystal structure; pyrrolidine; Hirshfeld surface analysis; NCI plots; computational chemistry.

CCDC reference: 2009242

Supporting information: this article has supporting information at journals.iucr.org/e

The title compound, $C_{23}H_{24}N_2O_9$, is a tetra-substituted pyrrolidine derivative with a twisted conformation, with the twist evident in the C—C bond bearing the adjacent acetyloxy substituents. These are flanked on one side by a C-bound 4-methoxyphenyl group and on the other by a methylene group. The almost sp^2-N atom [sum of angles = 357°] bears a 4-nitrobenzyloxycarbonyl substituent. In the crystal, ring-methylene-C—H···O(acetyloxy-carbonyl) and methylene-C—H···O(carbonyl) interactions lead to supramolecular layers lying parallel to $(\bar{1}01)$; the layers stack without directional interactions between them. The analysis of the calculated Hirshfeld surfaces indicates the combined importance of H···H (42.3%), H···O/O···H (37.3%) and H···C/C···H (14.9%) surface contacts. Further, the interaction energies, largely dominated by the dispersive term, point to the stabilizing influence of H···H and O···O contacts in the inter-layer region.

1. Chemical context

The structure of the title tetra-substituted pyrrolidine derivative, (I), was determined in connection with our on-going structural studies characterizing key synthetic intermediates in the synthesis of various α-glucosidase inhibitors (Zukerman-Schpector *et al.*, 2017; Dallasta Pedroso *et al.*, 2020). α-Glucosidase inhibitors are an important class of drugs employed in the treatment of a variety of diseases such as cancer, cystic fibrosis, diabetes and influenza (Kiappes *et al.*, 2018; Dhameja & Gupta, 2019).

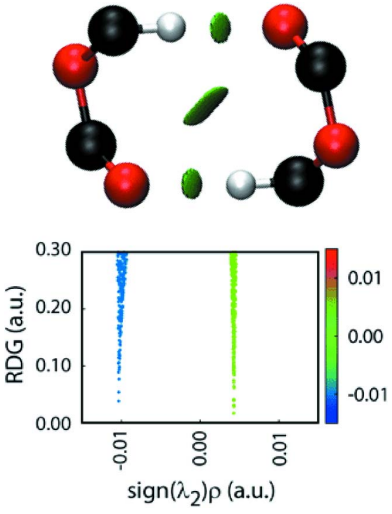

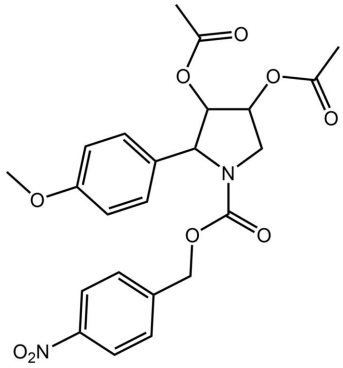

More specifically, (I) was generated during a study designed to synthesize the hydroxylated proline derivative, (2*R*,3*S*,4*R*)-3,4-dihydroxypyrrolidine-2-carboxylic acid, (II) (Garcia, 2008). In addition to being an α-glucosidase inhibitor, (II) is also found as a sub-structure of natural bioactive compounds such as, for example, a component of the repeated decapeptide sequence of the adhesive protein *Mytilus edulis foot protein 1* (Mefp1), which is produced by the marine mussel *Mytilus edulis* and is responsible for the fixation capacity of the mussel to rock (Taylor & Weir, 2000). The synthetic study determined that in the final stages of the reaction sequence towards (II), it was not possible to smoothly remove the N-bound 4-nitrobenzyloxycarbonyl (PNZ) protecting group *via* catalytic hydrogenation as the ensuing mixture was difficult to purify. Therefore, it proved necessary to remove the PNZ protecting group through acid hydrolysis at reflux temperature, resulting in a low overall yield (34%) suggesting that there was no advantage in using PNZ.

The crystal and molecular structures of (I) are described herein with this experimental study complemented by a detailed analysis of the molecular packing by a combination of Hirshfeld surface analysis, non-covalent interaction plots and computational chemistry.

2. Structural commentary

The molecular structure of (I), Fig. 1, is constructed about a tetra-substituted pyrrolidine ring with a N1-bound (4-nitrophenyl)ethylcarboxylate group and, respectively, C1–C3-bound 4-methoxyphenyl, acetyloxy and acetyloxy substituents. For the illustrated molecule, Fig. 1, the chirality of the C1–C3 atoms follows the sequence *R*, *R* and *S*, but it is noted that due crystal symmetry, the centrosymmetric unit cell contains equal numbers of the enantiomers. The conformation of the five-membered ring is twisted about the C2—C3 bond with the C1—C2—C3—C4 torsion angle being 39.70 (16)°, consistent with a (+)*syn*-clinal configuration. The sum of the angles about the N1 atom is 356.7°, indicating an approximate sp^2 centre.

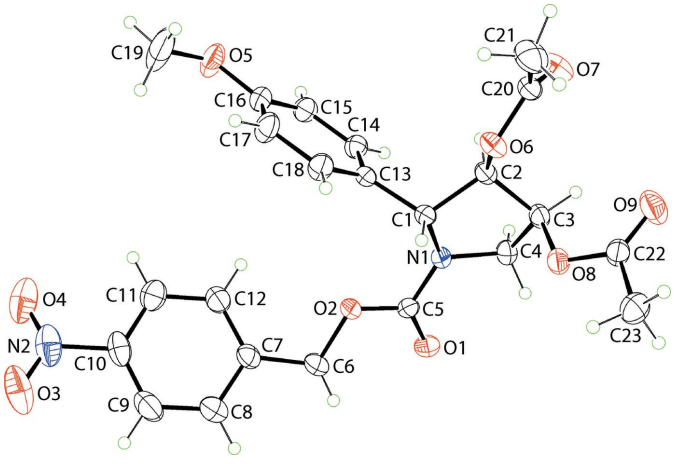

Figure 1
The molecular structure of (I), showing the atom-labelling scheme and displacement ellipsoids at the 35% probability level.

Table 1
Hydrogen-bond geometry (Å, °).

D—H···A	D—H	H···A	D···A	D—H···A
C4—H4B···O7^{i}	0.97	2.60	3.129 (2)	115
C6—H6A···O1^{ii}	0.97	2.54	3.250 (2)	130

Symmetry codes: (i) $-x+\frac{1}{2}, y-\frac{1}{2}, -z+\frac{3}{2}$; (ii) $-x+1, -y, -z+2$.

The N1-bound group occupies an equatorial position with those at the C1–C3 centres being bisectional, equatorial and axial, respectively (Spek, 2020). When viewed towards the approximate plane through the pyrrolidine ring, the N-bound carboxylate group is approximately co-planar, *i.e.* excluding the nitrobenzene residue. The C1-substituent lies to the opposite side of the plane than the C2 and C3-acetyloxy groups; the dihedral angle between the acetyloxy CO_2 planes is 57.7 (2)°.

With respect to the least-squares plane through the pyrrolidine ring, the nitrobenzene and methoxybenzene rings are splayed, as seen in the dihedral angles of 58.58 (8) and 77.65 (6)°, respectively; the dihedral angle between the benzene rings is 50.56 (5)°. There is a twist in the nitrobenzene ring as seen in the value of the C11—C10—N2—O4 torsion angle of 17.7 (3)°. By contrast, the methoxy group is co-planar with the ring to which it is connected, as shown by the C15—C16—O5—C19 torsion angle of 176.2 (2)°.

3. Supramolecular features

The only directional non-covalent interactions of note in the crystal of (I) are two weak C—H···O contacts as listed in Table 1. The presence of ring-methylene-C4—H···O7(acetyloxy-carbonyl) interactions lead to helical chains along the *b*-axis direction, being propagated by 2_1 symmetry. The other interactions falling within the distance criteria of *PLATON* (Spek, 2020) are methylene-C6—H···O1(carbonyl) interactions, formed between centrosymmetrically related (4-nitrophenyl)ethylcarboxylate groups, which lead to the formation of ten-membered $\{\cdots OCOCH\}_2$ synthons. These serve to connect the helical chains into a layer lying parallel to $(\bar{1}01)$, Fig. 2(*a*). A view of the unit-cell contents is shown in Fig. 2(*b*), highlighting the stacking of layers, without directional interactions between them.

4. Non-covalent interaction plots

The aforementioned weak C—H···O contacts identified in *Supramolecular features* were also evaluated by calculating non-covalent interaction plots (Johnson *et al.*, 2010; Contreras-García *et al.*, 2011). In short, these calculations indicate whether non-bonding contacts are attractive, weakly attractive or repulsive. The methylene-C6—H···O1(carbonyl) interactions giving rise to the ten-membered $\{\cdots OCOCH\}_2$ synthons are highlighted in the upper view of Fig. 3(*a*) with the green isosurface between the interacting atoms and the distinctive blue feature in the reduced density gradient (RDG)

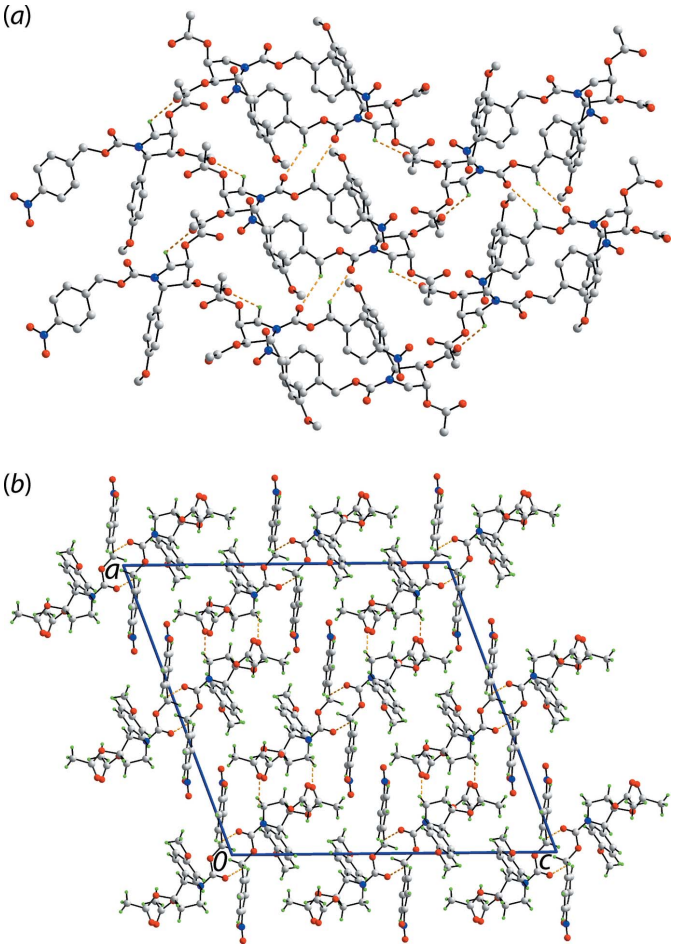

Figure 2
Molecular packing in (I): (*a*) supramolecular layer parallel to ($\bar{1}01$) sustained by methylene-C—H···O(carbonyl) contacts shown as orange dashed lines (non-participating H atoms are omitted) and (*b*) view of the unit-cell contents shown in projection down the *b* axis.

versus sign(λ^2)$\rho(r)$ plot in the lower view, *i.e.* indicating the density value is less than 0.0 a.u., suggest these interactions are weakly attractive. The same is true for the ring-methylene-C4—H···O7(acetyloxy-carbonyl) interactions that lead to the helical chain, Fig. 3(*b*).

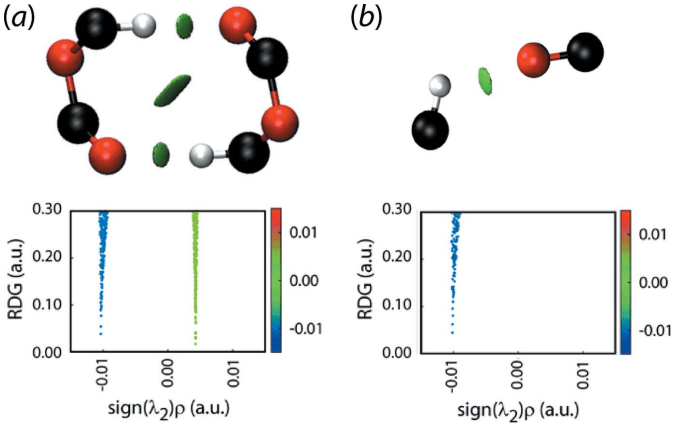

Figure 3
Non-covalent interaction plots for the following interactions in (I): (*a*) methylene-C6—H···O1(carbonyl) and (*b*) ring-methylene-C4—H···O7(acetyloxy-carbonyl).

Table 2
Summary of short interatomic contacts (Å) in (I)[a].

Contact	Distance	Symmetry operation
C6—H6*A*···O1[b]	2.47	$-x+1, -y, -z+2$
C4—H4*B*···O7[b]	2.55	$-x+\frac{1}{2}, y-\frac{1}{2}, -z+\frac{3}{2}$
C4···O7	3.13	$-x+\frac{1}{2}, y+\frac{1}{2}, -z+\frac{3}{2}$
C5···O5	3.08	$x, y-1, z$
O2···O5	3.02	$x, y-1, z$
C6—H6*B*···C15	2.73	$-x+1, -y+1, -z+2$
C9—H9···C21	2.75	$x+\frac{1}{2}, -y+\frac{1}{2}, z+\frac{1}{2}$
O4···O4	2.75	$-x+\frac{3}{2}, -y+\frac{3}{2}, -z+2$
H17···H23*B*	2.35	$-x+1, y+1, -z+\frac{3}{2}$

Notes: (*a*) The interatomic distances are calculated in *Crystal Explorer 17* (Turner *et al.*, 2017) whereby the *X*—H bond lengths are adjusted to their neutron values. (*b*) These interactions correspond to the interactions listed in Table 1.

5. Hirshfeld surface analysis

The Hirshfeld surface analysis of (I) involved the calculation of the d_{norm}-surface plots, electrostatic potential (calculated using the STO-3G basis set at the Hartree–Fock level of theory) and two-dimensional fingerprint plots following literature procedures (Tan *et al.*, 2019) using *Crystal Explorer 17* (Turner *et al.*, 2017). The weak methylene-C6—H···O1(carbonyl) interactions are reflected as bright-red spots near the methylene-H6*A* and carbonyl-O1 atoms on the d_{norm}-surface plot of (I) shown in Fig. 4. Additional diffuse red spots are also noted near the methoxy-O5 and carbonyl-O7 atoms in Fig. 4, which reflect their participation in short C5···O5 and C4···O7 contacts with separations ∼0.1 Å shorter than the sum of their van der Waals radii, Table 2. Further, faint spots near atom H4*B* as well as the O5 and O7 atoms (each difficult to discern in Fig. 4) are attributed to methylene-C4—

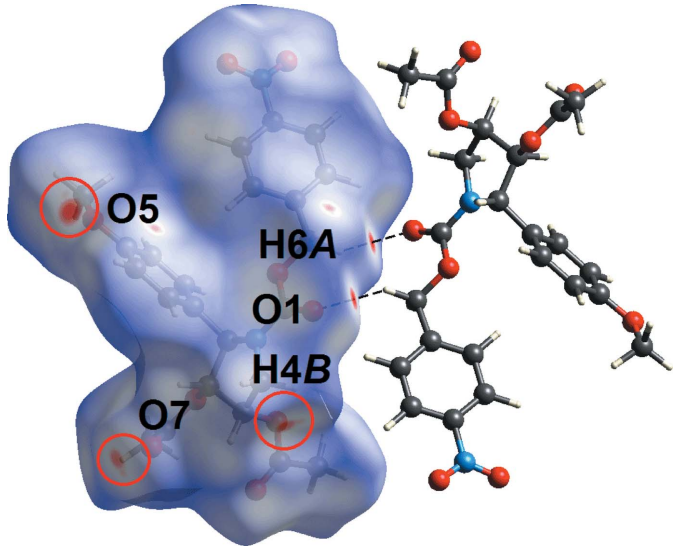

Figure 4
A view of the Hirshfeld surface mapped for (I) over d_{norm} in the range −0.090 to +1.583 arbitrary units showing the C—H···O interactions as black dashed lines.

Table 3
Percentage contributions of interatomic contacts to the Hirshfeld surface for (I).

Contact	Percentage contribution
H···H	42.3
H···O/O···H	37.3
H···C/C···H	14.9
O···O	2.1
O···C/C···O	1.2
Others	2.2

H4*B*···O7(carbonyl) and O2···O5 short contacts, being ∼0.02 Å shorter than their respective sums of the van der Waals radii, Table 2.

In the views of Fig. 5, the faint red spots that appear near the methylene (H6*B*), benzyl (C15 and H9), methyl (C21) and nitro (O4) atoms correspond to long-range intra-layer methylene-C6—H6*B*···C15(benzyl), benzyl-C9—H9···C21(methyl) interactions and inter-layer O4···O4 short contacts, Table 2. The Hirshfeld surface mapped over the electrostatic potential in Fig. 6 highlights the donors and acceptors of the indicated interactions through blue (positive electrostatic potential) and red (negative electrostatic potential), respectively.

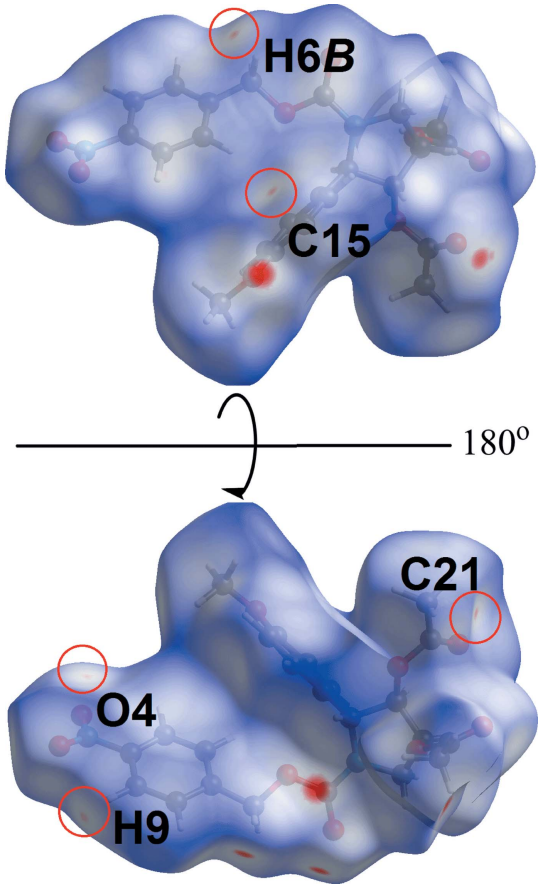

Figure 5
Two views of the Hirshfeld surface mapped over d_{norm} for (I) in the range −0.090 to +1.583 arbitrary units, highlighting evidence for long-range C—H···C interactions and O···O short contacts within red circles (see text).

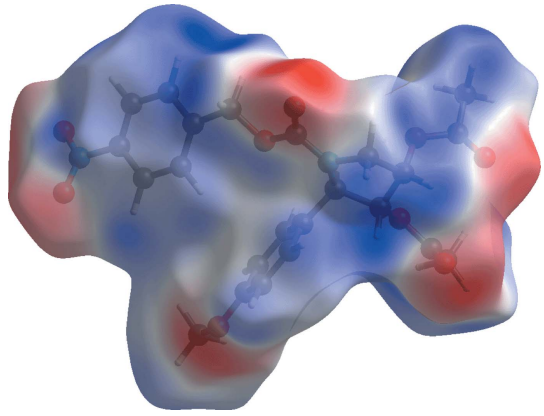

Figure 6
A view of the Hirshfeld surface mapped over the calculated electrostatic potential for (I). The potentials were calculated using the STO-3 G basis set at the Hartree–Fock level of theory over a range of −0.067 to 0.040 a.u. The red and blue regions represent negative and positive electrostatic potentials, respectively.

As illustrated in Fig. 7(*a*), the two-dimensional fingerprint plot for the Hirshfeld surface of (I) is shown in the upper left and lower right sides of the d_e and d_i diagonal axes, and those delineated into H···H, H···O/O···H, H···C/C···H, O···O and O···C/C···O contacts are illustrated in Fig. 7(*b*)–(*f*), respectively. The percentage contributions from different interatomic contacts are summarized in Table 3. The H···H contacts contribute 42.3% to the overall Hirshfeld surface with the shortest contact, manifested in the round-shape peak tipped at $d_e = d_i$ ∼2.4 Å, Fig. 7(*b*), corresponding to the H17···H23*B* inter-layer contact listed in Table 2. The H···O/O···H contacts contribute 37.3% to the overall Hirshfeld surface, reflecting the significant C—H···O contacts evident in the packing, Tables 1 and 2. The shortest contacts are reflected as two sharp spikes at $d_e + d_i$ ∼2.5 Å in Fig. 7(*c*). The H···C/C···H contacts that match the long-range C—H···C inter-

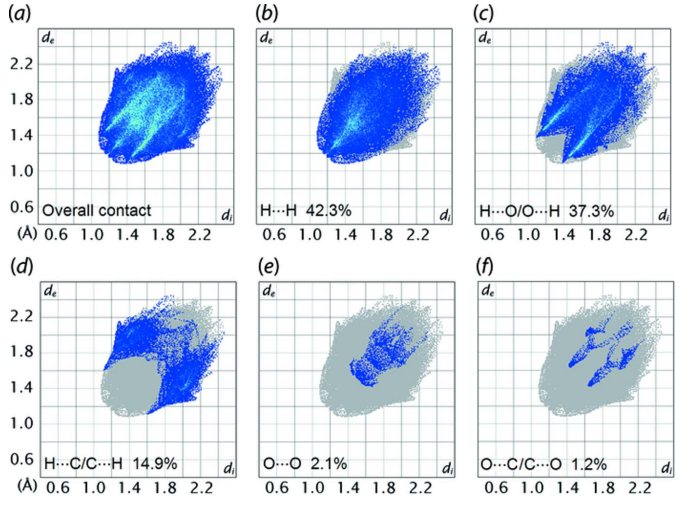

Figure 7
(*a*) The full two-dimensional fingerprint plot for (I) and (*b*)–(*f*) those delineated into H···H, H···O/O···H, H···C/C···H, O···O and O···C/C···O contacts, respectively.

Table 4
Summary of interaction energies (kJ mol^{-1}) calculated for (I).

Contact	R (Å)	E_{ele}	E_{pol}	E_{dis}	E_{rep}	E_{tot}
Intra-layer region						
C4—H4*B*···O7^{i} +						
C4···O7^{i}	10.99	−17.8	−6.1	−29.1	18.3	−37.3
C6—H6*A*···O1^{ii}	9.21	−23.8	−6.9	−23.2	21.7	−37.0
C5···O5^{iii} +						
O2···O5^{iii}	8.29	−8.4	−2.7	−56.3	29.1	−41.8
C9—H9···C21^{iv}	14.12	−12.7	−3.4	−20.5	12.0	−26.4
C6—H6*B*···C15^{v} +						
C4—H4*A*···O4^{v}	6.55	−18.1	−4.5	−87.1	52.8	−65.8
C21—H21*C*···O4^{vi}	15.04	−2.1	−1.0	−3.7	1.5	−5.2
Inter-layer region						
H17···H23*B*^{vii}	10.38	2.9	−1.2	−16.5	8.2	−7.1
H17···H21*B*^{vii} +						
H18···H21*B*^{viii}	6.24	−1.1	−1.6	−52.9	23.0	−34.2
O4···O4^{ix}	13.71	−16.1	−4.4	−16.2	10.8	−27.7
C8—H8···O3^{x}	12.70	−5.4	−1.3	−10.2	1.9	−14.4

Symmetry codes: (i) $-x+\frac{1}{2}, y-\frac{1}{2}, -z+\frac{3}{2}$; (ii) $-x+1, -y, -z+2$; (iii) $x, y-1, z$; (iv) $x+\frac{1}{2}, -y+\frac{1}{2}, z+\frac{1}{2}$; (v) $-x+1, -y+1, -z+2$; (vi) $x-\frac{1}{2}, -y+\frac{3}{2}, z-\frac{1}{2}$; (vii) $-x+1, y+1, -z+\frac{3}{2}$; (viii) $-x+1, y, -z+\frac{3}{2}$; (ix) $-x+\frac{3}{2}, -y+\frac{3}{2}, -z+2$; (*x*) $-x+\frac{3}{2}, -y+\frac{1}{2}, -z+2$.

actions discussed above are shown as a pairs of forceps-like tips at $d_e + d_i$ ~2.7 Å in the fingerprint plot delineated into H···C/C···H contacts, Fig. 7(*d*). Although both O···O and O···C/C···O contacts appear at $d_e + d_i$ ~3.0 Å in the respective fingerprint plots, Fig. 7(*e*) and (*f*), their contributions to the overall Hirshfeld surface are only 2.1 and 1.2%, respectively. The other interatomic contacts have a negligible effect on the molecular packing as their accumulated contribution is about 2.2%.

6. Energy frameworks

The pairwise interaction energies between the molecules in the crystal of (I) were calculated by summing up four energy components, comprising the electrostatic (E_{ele}), polarization (E_{pol}), dispersion (E_{dis}) and exchange-repulsion (E_{rep}) energies as per the literature (Turner *et al.*, 2017). In the present study, the energy framework of (I) was generated by employing the 6-31G(*d*,*p*) basis set with the B3LYP function. The individual energy components as well as the total interaction energies are collated in Table 4. As anticipated, the dispersive component makes the major contribution to the interaction energies owing to the absence of conventional hydrogen bonding in the crystal. The most significant stabilization energies are found in the intra-layer region and arise from the directional contacts outlined in *Hirshfeld surface analysis* as well as two additional C—H···O interactions, *i.e.* methylene-C4—H4*A*···O4(nitro) and methyl-C21—H21*C*···O4(nitro) with H···O separations of 2.63 and 2.77 Å, respectively.

The stabilization energies in the inter-layer region are also dominated by the E_{dis} terms associated with the H···H contacts as well as the long-range C—H···O interactions (−14.4 kJ mol^{-1}). For the former, the maximum energy is not found for the shortest H17···H23*B* contact (−7.1 kJ mol^{-1}), Table 2 and Fig. 8(*b*), but rather for a pair of benzene-H···H(methyl) interactions occurring in close proximity in a hydrogen-rich region but at longer separations (−34.2 kJ mol^{-1}). For the inter-layer O4···O4 contact mentioned above, there are almost equal contributions from E_{ele} and E_{dis}, Table 4, giving rise to a total interaction energy of −27.7 kJ mol^{-1}. The magnitudes of intermolecular energies are represented graphically in Fig. 8, and clearly demonstrate the dominance of the E_{dis} in the molecular packing.

7. Database survey

There are relatively few related structures having a similar substitution pattern to the tetra-substituted pyrrolidine ring of (I). The chemical diagrams for the two most closely related structures, (III), which has two hydroxyl substituents rather than acetyloxy (ALAVOA; Qian *et al.*, 2016), and (IV), which has more complex substituents (RAJDUC; Coleman *et al.*, 2004), are shown in Fig. 9.

8. Synthesis and crystallization

To a solution of 4-nitrobenzyl (2*S*,3*S*,4*R*)-3,4-dihydroxy-2-(4-methoxyphenyl)pyrrolidine-1-carboxylate (602 mg,

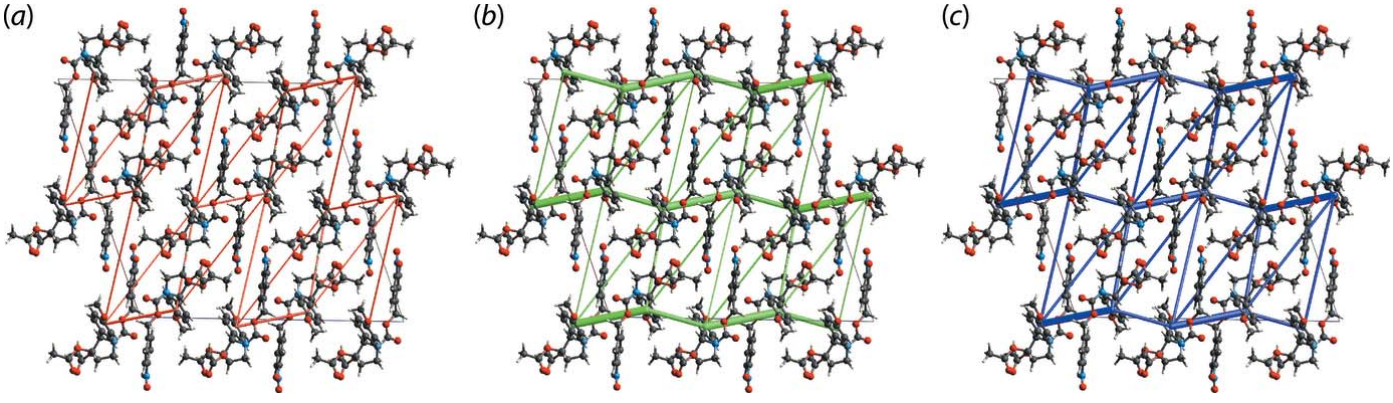

Figure 8
Perspective views of the energy frameworks calculated for (I) and viewed down the *b* axis showing (*a*) electrostatic potential force, (*b*) dispersion force and (*c*) total energy. The radii of the cylinders are proportional to the relative magnitudes of the corresponding energies and were adjusted to the same scale factor of 50 with a cut-off value of 5 kJ mol^{-1} within 1 × 1 × 1 unit cells.

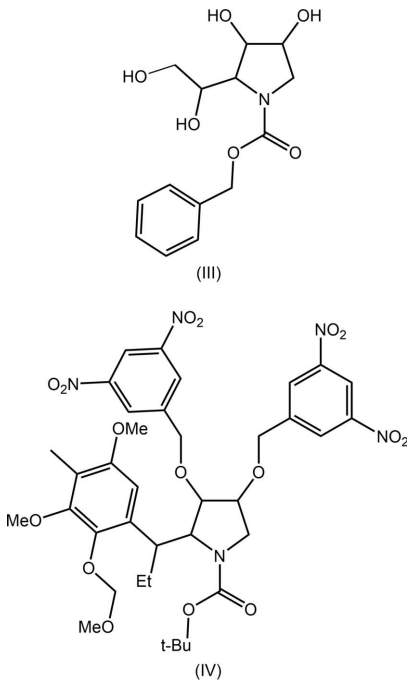

Figure 9
Chemical diagrams for (III) and (IV).

1.55 mmol) in CH_2Cl_2 (15 ml) were added pyridine (0.80 ml, 18.584 mmol), acetic anhydride (3.00 ml, 31.8 mmol) and *N*,*N*-dimethyl-4-aminopyridine (2.00 mg, 0.0164 mmol). The solution was stirred for 2 h at room temperature, concentrated in a rota-evaporator and the residue dissolved in EtOAc (10 ml). The resulting solution was washed with a HCl 5% solution (3 × 5 ml) and with saturated solutions of $NaHCO_3$ (2 × 5 ml) and of NaCl (5 ml). The phases were separated and the organic phase was dried with anhydrous Na_2SO_4, filtered and concentrated *in vacuo*.

The residue was purified by flash column chromatography in silica gel, using an EtOAc/*n*-hexane elution gradient (1:3 and 1:2). Yield: 716 mg (98%). Colourless irregular crystals for the X-ray analysis were obtained by the slow evaporation of its *n*-hexane solution. M.p. 409.5–410.5 K. The ^{1}H and ^{13}C{^{1}H} NMR reflect the presence of two conformational rotamers in solution. ^{1}H NMR (500 MHz, C_6D_6): δ = 7.75 (*d*, *J* = 7.3 Hz, 0.4H); 7.65 (*d*, *J* = 7.9 Hz, 1.2H); 7.18 (*m*, 1.9H); 6.99 (*d*, *J* = 7.9 Hz, 1.1H); 6.76 (*d*, *J* = 7.0 Hz, 0.5H); 6.72 (*d*, *J* = 7.3 Hz, 0.6H); 6.65 (*d*, *J* = 7.9 Hz, 1.3H); 6.37 (*d*, *J* = 9.3 Hz, 1H); 5.42 (*s*, 0.2H); 5.33 (*m*, 1.9H); 5.00 (*s*, 0.5H); 4.92 (*d*, *J* = 13.7 Hz, 0.6H); 4.74 (*s*, 0.6H); 4.44 (*d*, *J* = 13.7 Hz, 0.6H); 3.89 (*m*, 1.8H); 3.72 (*s*, 0.3H); 3.29 (*s*, 3H); 3.35–3.23 (*m*, 0.3H); 1.61–1.60 (2*s*, 6H). ^{1}H NMR (500 MHz, $CDCl_3$, TMS r.t.): δ = 8.23 (*d*, *J* = 8.2 Hz, 0.6H); 8.00 (*d*, *J* = 8.2 Hz, 1.2H); 7.53 (*d*, *J* = 7.9 Hz, 0.7H); 7.16 (*m*, 2H); 6.96 (*d*, *J* = 8.5 Hz, 1.2H); 6.88 (*d*, *J* = 8.5 Hz, 2.0H); 5.45–5.32 (*m*, 1H); 5.31–5.18 (*m*, 2.3H); 5.01–4.87 (*m*, 1.6H); 4.13 (*m*, 0.3H); 4.06 (*dd*, *J* = 11.6 Hz and 6.4 Hz, 0.7H); 3.85–3.67 (*s* + *m*, 4.1H); 2.12-2.07 (4*s*, 6H). ^{13}C{^{1}H} NMR (125 MHz, $CDCl_3$, r.t.): δ = 169.9; 169.8; 159.4; 159.2; 154.2; 154.1; 147.6; 147.2; 143.6; 143.4; 130.6; 129.4; 128.1; 127.5; 126.8; 126.7; 123.7; 123.4; 114.2; 78.2; 69.2; 68.7; 65.7; 65.5; 64.7; 64.1; 55.3; 55.2; 49.0; 48.4; 20.8; 20.7; 20.6.

Table 5
Experimental details.

Crystal data	
Chemical formula	$C_{23}H_{24}N_2O_9$
M_r	472.44
Crystal system, space group	Monoclinic, *C*2/*c*
Temperature (K)	293
a, *b*, *c* (Å)	23.6396 (5), 8.2906 (2), 24.7683 (5)
β (°)	110.013 (1)
V (Å^3)	4561.13 (18)
Z	8
Radiation type	Mo *K*α
μ (mm^{-1})	0.11
Crystal size (mm)	0.40 × 0.36 × 0.18
Data collection	
Diffractometer	Enraf–Nonius TurboCAD-4
Absorption correction	Multi-scan (*SADABS*; Sheldrick, 1996)
T_{min}, T_{max}	0.686, 0.745
No. of measured, independent and observed [$I > 2\sigma(I)$] reflections	22357, 4172, 3646
R_{int}	0.020
(sin $\theta/\lambda)_{max}$ (Å^{-1})	0.603
Refinement	
$R[F^2 > 2\sigma(F^2)]$, $wR(F^2)$, *S*	0.041, 0.112, 1.01
No. of reflections	4172
No. of parameters	310
H-atom treatment	H-atom parameters constrained
$\Delta\rho_{max}$, $\Delta\rho_{min}$ (e Å^{-3})	0.30, −0.22

Computer programs: *CAD-4 EXPRESS* (Enraf–Nonius, 1989), *XCAD4* (Harms & Wocadlo, 1995), *SIR2014* (Burla *et al.*, 2015), *SHELXL2018/3* (Sheldrick, 2015), *ORTEP-3 for Windows* (Farrugia, 2012), *MarvinSketch* (ChemAxon, 2010), *DIAMOND* (Brandenburg, 2006) and *publCIF* (Westrip, 2010).

9. Refinement details

Crystal data, data collection and structure refinement details are summarized in Table 5. The carbon-bound H atoms were placed in calculated positions (C—H = 0.93–0.98 Å) and were included in the refinement in the riding model approximation, with U_{iso}(H) set to 1.2–1.5U_{eq}(C).

Funding information

The Brazilian agencies Coordination for the Improvement of Higher Education Personnel, CAPES, Finance Code 001 and the National Council for Scientific and Technological Development (CNPq) are acknowledged for grant Nos. 312210/2019–1, 433957/2018–2 and 406273/2015–4 to IC, for a fellowship 303207/2017–5 to JZS and a scholarship to SDP. Sunway University Sdn Bhd is also thanked for funding (grant No. STR-RCTR-RCCM-001–2019).

References

Brandenburg, K. (2006). *DIAMOND*. Crystal Impact GbR, Bonn, Germany.
Burla, M. C., Caliandro, R., Carrozzini, B., Cascarano, G. L., Cuocci, C., Giacovazzo, C., Mallamo, M., Mazzone, A. & Polidori, G. (2015). *J. Appl. Cryst.* **48**, 306–309.
ChemAxon (2010). *Marvinsketch*. http://www.chemaxon.com.
Coleman, R. S., Felpin, F.-X. & Chen, W. (2004). *J. Org. Chem.* **69**, 7309–7316.

Contreras-García, J., Johnson, E. R., Keinan, S., Chaudret, R., Piquemal, J.-P., Beratan, D. N. & Yang, W. (2011). *J. Chem. Theory Comput.* **7**, 625–632.
Dallasta Pedroso, S., Caracelli, I., Zukerman-Schpector, J., Soto-Monsalve, M., De Almeida Santos, R. H., Correia, C. R. D., Llanes Garcia, A. L., Kwong, H. C. & Tiekink, E. R. T. (2020). *Acta Cryst.* E**76**, 967–972.
Dhameja, M. & Gupta, P. (2019). *Eur. J. Med. Chem.* **176**, article No. 343e377.
Enraf–Nonius (1989). *CAD-4 EXPRESS*. Enraf–Nonius, Delft, The Netherlands.
Farrugia, L. J. (2012). *J. Appl. Cryst.* **45**, 849–854.
Garcia, A. L. L. (2008). PhD thesis, Universidade Estadual de Campinas, UNICAMP, Campinas, SP, Brazil.
Harms, K. & Wocadlo, S. (1995). *XCAD4*. University of Marburg, Germany.
Johnson, E. R., Keinan, S., Mori-Sánchez, P., Contreras-García, J., Cohen, A. J. & Yang, W. (2010). *J. Am. Chem. Soc.* **132**, 6498–6506.
Kiappes, J. L., Hill, M. L., Alonzi, D. S., Miller, J. L., Iwaki, R., Sayce, A. C., Caputo, A. T., Kato, A. & Zitzmann, N. (2018). *Chem. Biol.* **13**, 60–65.
Qian, B.-C., Kamori, A., Kinami, K., Kato, A., Li, Y.-X., Fleet, G. W. J. & Yu, C.-Y. (2016). *Org. Biomol. Chem.* **14**, 4488–4498.
Sheldrick, G. M. (1996). *SADABS*. University of Göttingen, Germany.
Sheldrick, G. M. (2015). *Acta Cryst.* C**71**, 3–8.
Spek, A. L. (2020). *Acta Cryst.* E**76**, 1–11.
Tan, S. L., Jotani, M. M. & Tiekink, E. R. T. (2019). *Acta Cryst.* E**75**, 308–318.
Taylor, C. M. & Weir, C. A. (2000). *J. Org. Chem.* **65**, 1414–1421.
Turner, M. J., Mckinnon, J. J., Wolff, S. K., Grimwood, D. J., Spackman, P. R., Jayatilaka, D. & Spackman, M. A. (2017). *Crystal Explorer 17*. The University of Western Australia.
Westrip, S. P. (2010). *J. Appl. Cryst.* **43**, 920–925.
Zukerman-Schpector, J., Sugiyama, F. H., Garcia, A. L. L., Correia, C. R. D., Jotani, M. M. & Tiekink, E. R. T. (2017). *Acta Cryst.* E**73**, 1218–1222.